High-throughput CRISPR-mediated 3D enrichment platform for functional interrogation of chemotherapeutic resistance

Taraka Sai Pavan Grandhi*,#, Jeremy To, Angelica Romero, Fabio Luna, Whitney Barnes, John Walker, Rita Moran, Robbin Newlin, Loren Miraglia, Anthony P. Orth and Shane R. Horman

Genomics Institute of the Novartis Research Foundation, San Diego, CA 92121, USA.

(*) Present address - GlaxoSmithKline, Collegeville, PA, 19426

(#) Corresponding author email address: Tarakasaipavan.x.grandhi@gsk.com

Abstract

Cancer is a disease of somatic mutations. These cellular mutations compete to dominate their microenvironment and dictate the disease outcome. While a therapeutic approach to target specific driver mutations helps to manage the disease, subsequent molecular evolution of tumor cells threatens to overtake therapeutic progress. There is need for rapid, high-throughput, unbiased in-vitro discovery screening platforms that capture the native complexities of the tumor and rapidly identifiy mutations that confer chemotherapeutic drug resistance.Taking the example of CDK4/6 inhibitor (CDK4/6i) class of drugs, we show that the pooled in-vitro CRISPR screening platform enables rapid discovery of drug resistance mutations in a 3D setting. Gene edited cancer cell clones assembled into an organotypic multicellular tumor spheroid (MCTS), exposed to CDK4/6i caused selection and enrichment of the most drug resistant phenotype in a 3D setting, detectable by next gen sequencing after a span of 28 days. The platform was sufficiently sensitive to enrich for even a single drug resistant cell within a large, 2500-cell, drug-responsive complex 3D tumor spheroid. The genome-wide 3D CRISPR-mediated knockout screen (>18,000 genes) identified several genes whose disruptions conferred resistance to CDK4/6i. Further, multiple novel candidate genes were identified as top hits only in the microphysiological 3D enrichment assay platform and not the conventional 2D assays. Taken together, these findings suggest that including phenotypic 3D resistance profiling in decision trees could improve discovery and reconfirmation of drug resistance mechanisms and afford a platform for exploring non-cell autonomous interactions, selection pressures, and clonal competition.

Keywords: 3D tumor spheroids, high-throughput screening, drug resistance, pooled CRISPR screening, breast cancer

1. INTRODUCTION

Molecular-targeting chemotherapies exemplify precision medicine by exploiting and antagonizing key protumorigenic signaling pathways unique to specific clinical situations. Despite initial clinical successes, resistance often emerges upon prolonged exposure to targeted chemotherapies as either a manifestation of preexisting genetic mutations (de novo; primary resistance) or an accumulation of new mutations (acquired resistance) (Pao et al., 2005). Resistance mechanisms have typically been identified preclinically via ex vivo evolved resistance in cell lines (2D) or in mouse xenograft models, inducing drug resistance over a prolonged period of time (up to a year) (Garraway & Jänne, 2012; McDermott et al., 2014). However, these techniques often inadequately reproduce the complexity and heterogeneity of the tumor while also requiring significant investment in time and resources (Garraway & Jänne, 2012; Hoarau-Véchot, Rafii, Touboul, & Pasquier, 2018). Thus, there is a pressing need for new approaches for modeling resistance to targeted chemotherapeutics pre-clinically that ensure more faithful reproduction of complex tumor biology and better clinical relevance within a reasonable timeframe.

CDK4/6 inhibitors have achieved FDA approval for the treatment of estrogen receptor positive (ER+) human epidermal growth factor receptor 2 negative (HER2-) metastatic breast cancer in combination with hormone inhibitors (Fulvesterant or Letrozole) (Kwapisz, 2017). These drugs work by inhibiting phosphorylation activities of cyclin dependent kinases 4 and 6 (CDK4/6), which play crucial roles in early G1 cell cycle progression. CDK4/6 inhibition prevents RB1 phosphorylation and elicits G1 arrest and cellular stasis (Khleif et al., 1996). Antiestrogen hormone inhibitors similarly work to reduce cyclin D expression, furthering the impact of CDK4/6 inhibitor drugs (Sabbah, Courilleau, Mester, & Redeuilh, 1999). Multiple clinical trials have demonstrated the superiority of CDK4/6i and antiestrogen combinations relative to hormone inhibitors alone at extending the progression–free survival (Turner et al., 2018). Although these results are encouraging, emerging resistance mechanisms against CDK4/6 inhibition represent a threatening clinical challenge. Several modes of CDK4/6i resistance have been characterized

in the clinic including mutations in the exon sequences of the retinoblastoma gene, Cyclin D amplifications, and PI3K and/or mTOR amplification (Knudsen & Witkiewicz, 2017a).

Given the complexity, dynamism, and importance of the tumor microenvironment to drug-resistance mechanisms we sought to develop an *ex-vivo* cellular technology that models tumor-relevant drug resistance using CDK4/6 inhibition. Rapidly growing tumors harbor thousands of mutations at diagnosis that compete for space and nutrients influencing the emergence of acquired or inherent chemotherapy drug resistance mechanisms (Loeb, Loeb, & Anderson, 2003). We strove to create a technology that integrates competing somatic mutations within a complex 3D tumor environment under drug stress to identify likely phenotypes of CDK4/6i resistance. We sought to incorporate three key features into our *in-vitro* resistance screening platform: (1) tumor mutational burden and TME architecture that mimics *in-vivo* selection pressures, (2) rapid identification of clinically-relevant drug resistance pathways, and (3) automation-friendly implementation to enable genome-wide phenotypic scrutiny. To engineer TME architecture and biological complexity into the *ex-vivo* platform we employed 3D tumor spheroids (MCTS), which more faithfully mimic avascular and perivascular tumor regions (Grandhi, Potta, Nitiyanandan, Deshpande, & Rege, 2017; Horman et al., 2017). Differential zones of active cell proliferation, superior cell-cell interactions compared to 2D cultures, oxygen and nutrient gradients and drug diffusion properties found in solid tumors can be modeled in an actively growing 3D MCTS (Horman et al., 2017). In the case of ER+/Her2- luminal breast cancer, rapidly growing spheroids are pathologically mimetic of metastatic invasive ductal carcinoma, which is frequently characterized by a growing mass of epithelial-origin cells invading the nearby breast tissue out of the lumen of the milk duct, with likely central necrosis (Pervez & Khan, 2007). To mimic competing mutational events, we employed pooled CRISPR screening that uses large pools of lentiviruses to transduce cancer cells for altering gene expression in the context of a specific perturbagen (Chen et al., 2015; Szlachta et al., 2018). Further, 3D MCTS can be grown in multi-well formats, rendering them compatible to automation-friendly industrial workflows. We hypothesized that pooled CRISPR gene-edited cancer cells tightly packed into a 3D structure could mimic the diversity of

mutations competing within an actively growing solid tumor for dominance in the microenvironment under drug stress, resulting in the enrichment of the most resistant phenotype.

ER+ Her2- cancer cells with RB1 gene knockout (RBKO) (positive control) showed robust enrichment at a single cell level within a drug responsive 3D MCTS detectable after 28 days of CDK4/6i treatment. Combining microphysiological 3D MCTS with genome-wide pooled CRISPR genetic profiling under CDK4/6i stress identified novel drug-resistance mechanisms manifested through disruptions in the *SLC39A6* and *FAM134B* gene (Dai, Hua, & Hong, 2017; Sinn et al., 2019). CRISPR-mediated disruptions to the *SLC39A6* gene led to resistance against CDK4/6I and the combination CDK4/6i – Fulversterant mediated cytostasis. Further, this gene disruption target was identified as a top hit only in a 3D screen and not in the 2D counterpart control screen, indicating the differences and potential benefits of complex 3D platforms for rapid discovery of drug resistance mechanisms. Taken together, our results demonstrate a robust and novel 3D platform technology prognostic of clinically-relevant tumor phenotypes which may accelerate identification and development of novel combination therapeutic strategies.

2. METHODS

In-vitro 2D and 3D genome-wide pooled CRISPR screening against CDK4/6i

13.5 million T47D-Cas9 cells were plated in seven T225 flasks for 24 hours prior to addition of pooled virus (7 pools of Cellecta library) at an MOI = 0.5 with 8 µg/ml of polybrene. After 24 hours of virus addition, the media was refreshed with 2.5-3.0 µg/ml of puromycin selection marker. After 72 hours of selection, the media was refreshed for 24 hours and 5.3 million cells were isolated for baseline sequencing. 5.3 million cells were further placed into T225 2D flasks or added to Corning 384w ULA plates at 2500 cells per well. 1 µM of CDK4/6i was added to the 2D and 3D plates after 4 days of 2D culture and spheroid formation respectively. The media was then refreshed every 4 days with fresh 1 µM drug. The 2D cells were sampled on days 10, 18, 22 and 28 (days 6, 12, 18, and 24 after drug addition) (one half), whereas 3D spheroids were

collected on day 28 after cell culture in ULA plates (d24 after drug addition). A time-dependent enrichment map was created to compare 2D and 3D enrichment cultures.

3. RESULTS

ER+ Her2- cells form 3D MCTS, mimic clinical tumor pathology and sensitivity to CDK4/6i

Human luminal ER+ Her2- breast cancer T47D cells were engineered to express the Cas9 protein. These cells showed robust, uniform formation of 3D multicellular tumor spheroids (MCTS) which exhibited continuous growth over a 20 day study period (Fig. 1a). Utilizing 384-well high-content spheroid plates enabled the scrutiny of high numbers of 3D spheroids in an automated and robust manner, which increased significance scores of subtle growth phenotypes (Fig. 1a). H&E staining of 3D MCTS sectioned on days 4 and 20 after cell seeding showed the development of Ki67+ proliferation zones and central necrosis (Fig. 1b), demonstrating the potential of T47D spheroids to mimic the hierarchical organization of luminal breast tumors. There were no apparent differences in growth kinetics between the T47D-Cas9 cells used here and non-Cas9-expressing T47D cells (data not shown). Exposure of T47D-Cas9 spheroids to the CDK4/6 inhibitor drug over 20 days showed a concentration-dependent reduction in cell number and spheroid volume (Fig 1c), indicating spheroid volume could be used as a functional metric to quantitate drug sensitivity. At high CDK4/6i concentrations, transmitted light images showed highly dense and necrotic spheroid structures (Fig. 1c, 100 μM). Exposure of CDK4/6i drug to the 3D T47D MCTS led to its accumulation in punctated bodies in cell cytoplasm which continued to concentrate over 12 hours (Fig. 1d). The GI(50) values – the drug concentrations required for 50% cytostasis - were higher in 3D MCTS than 2D for CDK4/6i (Fig. S1 a,c,e). GI: Growth Inhibition value. However, overall T47D-Cas9 cells showed higher sensitivity to CDK4/6i compared to CDK4/6i_2 drug, a similar CDK4/6-targeting drug (Figure S1).

CRISPR-mediated RB1 knockout confers treatment-relevant resistance to CDK4/6i

The emergence of inactivating or oblative somatic mutations of RB1 after treatment with targeted CDK4/6i has been observed in the clinic in metastatic breast tumor patients (Knudsen &

Witkiewicz, 2017b). To test if RB1 mutations phenocopy drug resistance in our assay platform, we generated retinoblastoma protein knockouts (KOs) by CRISPR to mimic the downstream effects of clinically-observed mutations that lead to protein loss. Retinoblastoma knockouts generated by CRISPR showed robust knockout/deletion of the protein (RB1 KOs) as detected by western blot compared to scrambled and live controls (Fig 2a). T47D-Cas9 RB1 KO cells, when seeded in round bottom ULA plates continued to make 3D MCTS (Fig 2a). When tested for CDK4/6i resistance in the 3D spheroid assay, RB1 KO clones showed significant resistance to CDK4/6i compared to live and scrambled sgRNA controls (Fig 2a). In 2D culture, the average cell numbers of RB1 KOs were significantly higher compared to T47D-Cas9 live and scrambled controls at both 1μM and 10μM drug concentrations, indicating loss of cytostatic activity of the drug after RB deletion (Fig. 2b and S2a). These results indicate the potential of this 3D high-throughput platform to phenocopy clinically-relevant phenotypes in vitro. A comparison of 2D vs. 3D assay systems for drug sensitivity indicated that the RB1 KO cells were significantly more sensitive to the drug in 2D compared to the 3D format (Fig S2 a-b). While RB1 KO cells were differentially sensitive to increasing concentrations of CDK4/6i in a 2D setting (1μM vs. 10μM), the volumes of RB1 KO spheroids were not significantly different between 1μM and 10μM (Fig S2 a-b), indicating a differential response to the same drug in 2D vs 3D.

To confirm the correlation between spheroid volume and cell viability, we performed a CellTiter-Glo assay on T47D spheroids exposed to CDK4/6i. We observed a strong positive correlation between cell viability and spheroid volume indicating spheroid volume can serve as a surrogate metric for quantifying resistance to CDK4/6 inhibitor drugs (Fig. S2c).

3D assay platform can enrich for low numbers of drug-resistant cells within a sensitive tumor spheroid

To characterize the ability of the spheroid/CRISPR assay platform to detect small numbers of drug-resistant cells within a large drug-sensitive 3D MCTS, we performed a limiting dilution study using RB1 KO cells. 3D spheroids generated with ratios of 1:1 or 1:10 RB1 KO : Scr con-

trol (drug resistant : drug sensitive) showed significant enrichment in spheroid size over spheroids generated with scrambled controls alone (Fig. S3a-c). To further mimic a clinical setting where very small numbers of drug-resistant cells would emerge from a treated tumor and to quantify those numbers, RB1 KO clones demonstrating CDK4/6i resistance were diluted within large spheroids comprised of control T47D cells. Tumor spheroids containing 160 resistant RB1 KO cells within a 2500 sensitive cell population started showing visible signs of enrichment as noted by protruding oval edges starting day 16. Surprisingly, spheroids containing only 2 drug-resistant RB1 KO cells produced a small bud on day 20 as seen by the outgrowth from the cytostatic spheroid that became significantly clear on day 24 (Fig. 2c). Quantification of spheroid size indicated that low drug-resistant cell number spheroids do not show any significant changes until day 20, at which time there is a visual enrichment for resistance (Fig 2c). In contrast, increasing the number of resistant cells in resistant : sensitive spheroids (80, 40, 20, 10 and 5 resistant cells) yielded visible outgrowths as early as day 12 or day 16 (Fig. S4). Sectioning and staining of 2-cell resistant spheroids for the proliferation marker Ki67 showed that cell proliferation is limited to the detectable budding outgrowth, confirming that only the RB1 KO cells could proliferate and enrich within a cytostatic spheroid during the 24 days of exposure to CDK4/6i (Fig 2d). Similar phenotypes were seen using the other pRB1 CRISPR KO cell clones (data not shown). At lower levels of cell titration, some spheroids showed two detectable outgrowths indicating the propensity of the resistant cell clones to grow out even if present further away from each other within the sensitive spheroid (Figure S5a).

To ascertain if the assay platform was sensitive enough to detect only a single drug-resistant cell among a 3D tumor mass of 2500 drug-sensitive cells we performed the same assay using 1 RB1 KO cell per spheroid. Though minor enrichment was evident in 24 days, 28 days was essential to record significant outgrowths in the one RBKO-cell-per spheroid system in all positively enriched spheroids (Fig. S5b). After 28 days of enrichment, single cell outgrowths from drug sensitive spheroids were observed for both RB1 KO2 and RB1 KO3, and a higher percentage of outgrowths were seen in RB1 KO2. Further, a concentration-dependent effect was observed in

fractions of wells with detectable outgrowths. 28 day treatment with 1 μM drug led to slightly higher percentages of wells with detectable outgrowths (Fig. S5c-d).

To quantify gross contributions of the two cell populations (RBKO versus $RB^{WT/WT}$) we sequenced whole spheroids made from one RBKO cell per spheroid for the RB knockout, determining that after after 28 days of enrichment under CDK4/6i drug stress over 70% of the reads originated from proliferating RB1 KO cells (Fig. 2e). These data, when considered together, indicate in-vitro enrichment of very low numbers of drug-resistant clones within a 3D spheroid are achievable in a high-throughput, screenable format enabling a genome-wide functional probing for novel resistance mechanisms against CDK4/6 inhibition.

Genome-wide 3D in vitro pooled CRISPR screening identifies known and novel resistance mechanisms to CDK4/6 inhibition

Identification of novel mechanisms of drug resistance is critical for proactively exploring alternative therapeutic strategies. By combining genome-wide pooled CRISPR screening with 3D organotypic multicellular tumor spheroids (MCTS) to perform functional phenotypic profiling for drug-resistance, we were able to enrich and select for CDK4/6i-resistant clones whose edited loci can be identified (Fig. S6). Based on our previous assay optimization, drug exposed whole 3D MCTS were collected directly for sequencing on day 28 (Fig. 3a). To assess similarities and differences between the 2D and 3D screening approaches, we also collected cells for sequencing on days 10, 16, 22 and 28 after drug addition in 2D format as well (Fig. 3a). Moreover, because the assay is rooted in the ability of CDK4/6i-resistant cells to outproliferate those whose growth is halted by CDK4/6i inhibitors, the assay is specifically tailored to reveal cytostasis resistance mechanisms (example: RB1 knockouts) by quantifying enrichment in resistant cell numbers over baseline under prolonged drug stress. 1 μM CDK4/6i was chosen instead of 10 μM to allow for less-stringent enrichment of the drug resistant clones (A dosage likely 10 fold higher than the clinically achieved C_{max}) (Liston & Davis, 2017) . A drug concentration of 1 μM previously indicated higher percentages of outgrowths during assay optimization (Fig. S5c-d).

7 pools of CRISPR single guide RNA (sgRNA) libraries covering 19,000 genes were employed to screen through 20,000 3D spheroids at sufficient coverage of guides to ensure that each guide was represented an average of 400 times. Upon visual analysis, two distinct positive enrichment phenotypes were observed, one characterized by dumbbell-shaped spheroids harboring a singular outgrowth (similar to RB1 KO mediated resistance) and a second characterized by large spheroids (Fig. 3b). Subsequent pooling of the spheroids, genomic DNA isolation, and index barcode sequencing enabled identification of the guides enriched in these samples.

The 3D spheroid genome-wide functional genomics screen identified existing and novel genes whose knockout led to CDK4/6 inhibitor resistance (Fig. 3c,d). RB1 deletion was observed as a significantly-enriched hit during the study, recapitulating a clinically-relevant resistance mechanism in our in vitro system. The screen also identified two genes with no previous linkage to the emergence of CDK4/6 inhibitor resistance: the cell surface zinc transporter *SLC39A6* and the ER resident selective autophagy receptor *FAM134B*.

Comparative analysis of 2D and 3D pooled in-vitro enrichment

Time course enrichment from the concurrent 2D screen indicated that the enrichment profiles of 2D vs 3D assays are profoundly different regardless of the time point (Fig 3c, S7a,b). Though the RB1 knockout control was not identified on day 10 in the 2D assay, RB1 KO was identified as one of the most enriched hits in 2D by day 16 (Fig. S7a,b). In fact, RB1 KO was identified as the only major hit from the 2D enrichment screen at the end of 28 days (Fig. S7a). While RB1 KO was identified in both 2D and 3D screens, a head-to-head comparison of the enrichment ratio of RB sgRNAs indicated a significant difference between the two assay formats (Fig. S7c). The enrichment ratio of RB1 sgRNAs in 2D screen was approximately 14 fold higher than the 3D screen ($p<0.05$, unpaired t-test) indicating the widely different growth drivers in 2D and 3D formats; i.e. unlimited proliferative capacity in 2D tissue culture plates unlike 3D spheroids.

In 3D, three genes were significantly enriched: RB1, which also shows up in 2D, and *SLC39A6* and *FAM134B*, which did not show up as top hits in the 2D screen (Fig. 3c,d and S7d). Only

loss of RB1 yields resistance to CDK4/6i in both formats (Fig. S7d). An analysis of the top 20 genes most enriched in 3D indicated minimal selective enrichment in the 3D format. In other words, these CRISPR knockouts enrich in both 2D and 3D formats, but do not occur in top 20 most enriched list in 2D (Fig. S7d). A comparison of top 20 most genes enriched in 3D to time course 2D reflect the significant differences between 2D and 3D where, apart from RB1, there was no significant overlap between the two groups (top 20 genes only) (Fig. 3c, S7b,d). Hierarchial clustering of the top 20 hits in 3D format also reflected the significant divergence between both the groups (Fig. S7b). In addition to *SLC39A6*, other genes regulating zinc ion transport and homeostasis such as *SLC39A9 and SLC30A7* were also identified within the top 1% of most enriched genes in 3D (GO analysis via metascape) whose yieled CDK4/6i resistance (Fig. S7e). Knockout of genes in pyruvate metabolism, small GTPase mediated signal transduction and transport of organic acids, metal ions and amine compounds were other gene ontologies that were significantly enriched in the 3D screen (Fig. S7e). The entire enriched gene list in 2D and 3D assays are provided separately (Supplementary tables 1 and 2 respectively). These data indicate divergent selection pressures between the 2D and 3D assay formats that may account for the differential phenotypes observed. Taken together, our data show that the 3D HTS spheroid pooled in vitro CRISPR screening platform is a powerful tool for identifying novel drug resistance genes in a a rapid screenable manner.

SLC39A6 gene disruption induces resistance to CDK4/6 inhibitors

To better characterize and confirm the observed enrichment of SLC39A6 knockouts in our 3D resistance screen, we generated stable *SLC39A6* gene-edited T47D-Cas9 cell clones for subsequent studies. Sanger sequencing and subsequent sequence trace decomposition via TIDE analysis of SLC-KO2 and SLC-KO4 aligned to scrambled control revealed a heterogeneous population of insertions and deletions in the targeted regions of the *SLC39A6* locus (Fig. S8a-c). While SLC-KO2 clones showed a predominantly large population of single insertions (likely adenine) (~75-85% of population), cells treated with SLC-KO4 guides showed a heterogeneous population with approximately ~25% with a single insertion (Fig. S8a-c). Single nucleotide inser-

tion in SLC-KO2 clones (in exon 4 of *SLC39A6* gene led to a frameshift mutation and a premature stop codon, predicted to create a truncated protein with molecular weight of 15.9 KDa (Fig. S8d,e). Indeed, western blotting using cell membrane-enriched protein fractions isolated from the SLC-KO2 pooled population indicated presence of a similarly-sized truncated protein approximately 16 KDa which was clearly absent from the scrambled control (Fig. 4a). A faint band of 16 KDa was also observed in cell membrane-enriched fractions of SLC-KO4, indicating the minor population observed with the single insertion in this clone likely possess the truncated protein. However, two additional protein bands of full length protein were also observed across all samples indicating either a heterogeneously-edited population or incomplete editing at *SLC39A6* loci. These results indicate a strong correlation between observations recorded by sanger sequencing and western blotting (Fig. 4a and S8a-c).

In 2D assays, stable SLC-KO2 and SLC-KO4 cells demonstrated significant drug-resistance compared to scrambled control cells after 6 days of CDK4/6i exposure (Fig. 4b). SLC-KO2 spheroids also demonstrated slight yet significantly more resistance to drug compared to the scrambled control spheroids as observed by the increase in spheroid volume over 20 days of drug exposure at both concentrations of 1 and 2 μM (Fig. 4c). Single agent fulvesterant treatment elicited a similar response from the SLCKOs compared to the scrambled control cells in the 2D and 3D assay (Fig. 4d,e). Resistance to cytostasis by SLC-KO2 cells compared to scrambled control cells was also observed in the 2D and spheres treated with the clinical combination of CDK4/6i plus fulvesterant (Fig. 4f). While the SLCKOs showed slight yet significant resistance to single agent drug treatments compared to the scrambled controls in 2D and 3D assays, the average numerical difference was higher in the combination treatment compared to the single agent treatments (Fig. 4b-f).

Previous studies have indicated the important role of SLC39A6 in importing zinc into the cell and maintainence of cellular zinc homeostasis (Ma et al., 2009). To better characterize the functional consequence of SLC39A6 protein loss on intracellular labile zinc levels, we quantitated labile zinc levels in SLC39A6 KO or scramble control cells using the zinc-binding Fluozin3-AM

dye. Surprisingly, we found that gene-edited T47D cells with the truncated version of SLC39A6 exhibited a significant 30% increase in the levels of intracellular labile zinc compared to those bearing the scrambled control (n=5 independent experiments) (Fig. S9a-e). To characterize the potential relationship between SLC39A6 and CDK4/6i-induced cell cycle arrest, we profiled cell cycle status of the SLC39A6 KOs and scrambled control cells after 48 hours of CDK4/6i treatment. We observed significant increases in the number of cells in the G2/M phase in SLC39A6 knockout samples compared to scrambled controls (Fig. S9b). These results indicate that the genetic editing of the *SLC39A6* locus and subsequent disruption of functional SLC39A6 cell membrane protein results in higher intracellular labile zinc accumulation and increased resistance to cell cycle arrest.

Exogenous delivery of zinc rescues cells from CDK4/6i induced cytostasis

As SLC-KO2 clones showed higher intracellular zinc levels and subsequent resistance to CDK4/6i cytostatic drugs, we artificially elevated the intracellular labile zinc to attempt to recreate the observed link between zinc and cytostasis in the presence of CDK4/6i. Artificial delivery of labile zinc achieved by exogenous delivery of zinc sulfate plus pyrithione [zinc ionophore (Kim et al., 1999)] resulted in a dose-dependent increase in intracellular zinc concentration within 15 minutes of exposure (Fig. 5a). A supra-physiological concentration of 20 μM zinc sulfate plus 10 μM pyrithione, applied to estimate intracellular zinc delivery potential, resulted in a significant increase of intracellular zinc concentration as noted in T47D-scrambled control cells (Fig. 5a). Longer exposure of T47D-scrambled control cells or MCF7-Cas9 cells to zinc sulfate plus pyrithione (6 days) at any concentrations above 0.1 μM (pyrithione) were found to be cytotoxic (Fig. S10a,b). Hence, we chose a 6 day dose response study of 1 μM zinc sulfate with pyrithione below 0.1 μM combined with different doses of CDK4/6i. Artificial elevation of intracellular labile zinc via delivery of pyrithione significantly rescued T47D-scrambled control cells and MCF7-Cas9 cells from CDK4/6i-induced cytostasis (Fig. 5b-c). Doses of 0.02 μM to 0.1 μM of pyrithione co-delivered with zinc sulfate rescued cells from CDK4/6i mediated cell cytostasis compared to the no zinc – no pyrithione control. (Fig. 5b-c).

Taken together, our results point to a high-throughput in-vitro platform technology capable of rapidly identifying targets with well-known and novel modes of resistance to clinically relevant chemotherapeutics that might be missed in conventional 2D screens.

4. DISCUSSION

Predictive detection of drug-resistance mechanisms may allow for identification of prophylactic drug regimens that mitigate therapy relapse. Early detection of resistant mechanisms to novel anticancer drugs in the pipeline could also allow for identifying patients not likely responsive to a therapy. Recent clinical successes of CDK4/6 inhibitors for ER+ Her2- breast cancer have warranted further application of these drugs for other solid tumor indications (Pernas, Tolaney, Winer, & Goel, 2018). Although these drugs demonstrate significant clinical efficacies, mechanisms of drug-resistance have emerged in the clinic, leading to disease relapse (Knudsen & Witkiewicz, 2017a). Therefore, rapid identification of resistance mechanisms against CDK4/6 inhibition before they emerge in patients are of critical importance.

We sought to develop a novel high-throughput *in-vitro* platform technology that enables rapid discovery of anticancer drug-resistance phenotypes through the incorporation of treatment-relevant tumor selection pressures. Current models of identification of drug resistance via 2D cell exposure to mutagens, exposure to low drug concentration for lengthy periods of time (multiple months to a year) or serial passaging of tumor xenografts in mice (for a year), are either inadequate, lengthy, laborious, or detached from clinical translation (Garraway & Jänne, 2012).

3D spheroids have been previously used to probe CDK4/6i-mediated sensitivity and resistance (Bacevic et al., 2017). Bacevic et al. showed that spatial constriction of CDK4/6 resistant cells with CDK4/6 sensitive cells within 3D spheroids allows competition and control of tumor burden under low dose CDK inhibition, which was not observed in the 2D environment indicating the potential advantages of using the 3D system to study cytostatic anticancer therapies (Bacevic et al., 2017). Rapidly growing tumors, including luminal breast cancers, may harbor myriad mutations at the time of diagnosis. Treatment with a molecularly-targeted therapeutic alters the

stresses governing tumor growth, allowing for selection and expansion of new drug resistant phenotypes (Loeb, 2016; Loeb et al., 2003). Additionally, spontaneous mutations may also arise in a tumor under drug stress, leading to therapy resistance (Housman et al., 2014). Luminal breast tumors have been shown to suffer stresses of hypoxia, necrosis and nutrient deprivation, all whilst competing for available space and resources. Many of these features are similarly captured by culturing cancer cells as 3D multicellular tumor spheroids (Tomes et al., 2003). By combining clinically-relevant tumor stresses *in-vitro* with genome-wide functional profiling for resistance mediators, we can enrich for and rapidly identify drug resistance phenotypes, which can then be molecularly characterized.

Towards that, we hypothesized that combining genome-wide CRISPR edited cancer cells in a 3D MCTS system would allow for rapid identification of physiologically-relevant novel resistance mechanisms against novel anticancer drug stress such as CDK4/6i. Genome-wide CRISPR editing mediated mimicking of gain or loss of function allows unbiased identification of genotypes contributing to a desired phenotype under appropriate selection stress. Further, utilizing automated high throughput screening enabling technologies such as 384w ultra low attachment plates for spheroid formation allow standardized industrial workflows to achieve the desired experimental outcome. Similar genome-wide searches have led to identification of 3D specific growth vulnerabilities in non-small-cell lung carcinoma cell lines (Han et al., 2020). T47D 3D MCTS generated in HTS format displayed similar pathologies to *in-vivo* tumors, characterized by zones of cell proliferation and necrosis. While T47D ER+ Her2- breast cancer cells displayed sensitivity to CDK4/6i drugs in both 2D and 3D cell culture formats, they were found to be more sensitive to CDK4/6 inhibitors in 2D (GI50 value) (Fig. S1). As the primary mode of action of this drug is via cell cycle arrest, drug exposure gradients within 3D spheroids may account for this differential sensitivity (Tchoryk et al., 2019); a possibility further underscore by the similar observation that RB1 knockout cells demonstrated greater sensitivities to CDK4/6 inhibitor drugs under 2D growth conditions compared to 3D spheroid conditions (Fig. S2). Our results showed that the CDK4/6i drug, when applied to T47D 3D MCTS, was noted to accumulate in punctated

vesicles within the cells of the 3D spheroid shell (Fig. 1d). CDK4/6i drugs have been shown to preferentially accumulate in the acidic lysosomes of cancer cells, which further acts as a storage depot for temporal release of the drug (Llanos et al., 2019). It is tempting to speculate that this preferential accumulation of the drug concentrates higher amounts of it in certain locations of the spheroid (spheroid shell) leading to a decreased gradient of drug towards the core of the spheroid, resulting in increased resistance in 3D (Bacevic et al., 2017; Jove et al., 2019). Similar observations of differential drug sensitivity in 2D vs 3D have been noticed across multiple cancers and constitute one of the important features of 3D screening systems to mimic in-vivo relevant drug sensitivities (Imamura et al., 2015).

3D MCTS morphologies allowed for expansion of the fittest drug resistant phenotype from a single cell event (RB1 knockout) to a detectable outgrowth; and this selection was independent of neighboring sensitive cells which did not constrain drug-resistance mechanisms evolving deep within dying tumors. To the best of our knowledge, this is the first evidence of a *in-vitro* 3D anti-cancer drug resistance screening platform with sensitivities of detection reaching a single cell level. Hence, 3D multicellular spheroid morphologies allowed screening of competing mutations under drug stress to rapidly identify the most drug resistant phenotype. This strategy allowed us to quickly mimic the heterogeneous repertoire of mutations competing for dominance in patient tumors under drug stress (Angus et al., 2019). We identified two novel genes by genome-wide 3D CRISPR screen, *SLC39A6* and *FAM134B*, ranked 1 and 3 via the 3D enrichment score whose disruption conferred resistance to the cells under CDK4/6i drug stress. While enrichment of RB1 knockout (clinically relevant to inactivating RB1 mutations) was observed in both 2D and 3D in-vitro pooled CRISPR screens, vast differences were observed among other hits identified in 2D and 3D screening formats. Specifically, there was almost no overlap between 2D and 3D in enriched genes list indicating widely diverse selection and enrichment forces at play in these formats. For example, 3D screen hits of SLC39A6 and FAM134B, ranked 1 and 3 in 3D, were ranked 3557 and 191 respectively in the 2D screen. Though these hits were differently ranked in 2D vs 3D, there wasn't selective enrichment in 3D with these gene hits.

We performed a deeper characterization of the SLC39A6 gene edited cell clones. While the resistance to single agent treatment of CDK4/6i and fulvesterant was slight in comparison to the scrambled control, significantly higher window of resistance was observed against the combination of the drugs. *SLC39A6* codes for a plasma membrane resident zinc transporter (ZIP6), which is suspected to play a vital role in zinc import and regulation of intracellular zinc homeostasis, and has been shown to be highly expressed in luminal breast cancer cells (Ma et al., 2009). Overexpression of *SLC39A6* has been associated with less aggressive ER+ tumors, longer relapse-free survival and overall survival (OS) (Kasper et al., 2005), while loss of *SLC39A6* has been associated with resistance against HDACi (Vorinostat) and epithelial to mesenchymal transition (Lopez & Kelleher, 2010; Ma et al., 2009). Further, a recent study correlated high expression of *SLC39A6* with longer PFS (progression free survival) and OS (overall survival) for metastatic breast cancer patients treated with endocrine therapy (Sinn et al., 2019).

Our results reinforce the need to incorporate alternative complex 3D spheroid / organoid models into drug resistance identification workflows. While our 2D and 3D screen identified well known mechanism of resistance driven by RB1 mutations, certain well known mechanisms of CDK4/6i resistance were not detected in the 2D or 3D screen. PTEN loss is a well known mechanism of resistance observed in patients and loss of PTEN in T47D cells confers resistance to CDK4/6i (Costa et al., 2019). However, the screening platform failed to enrich PTEN knockouts likely due to either improper genetic editing via the guide RNAs, too few stably edited cells before the screen or a yet unknown mechanism. Our studies indicated a significant increase in intracellular zinc concentration after editing of *SLC39A6* loci, consistent with previous reports that have shown increases in intracellular labile zinc concentration after siRNA mediated knockdown of SLC39A6 (Ma et al., 2009). Further, two other genes *SLC39A9, SLC30A7* coding for proteins ZIP9 and ZnT7 were also identified within the top 1% most enriched hits in the pooled 3D CDK4/6i resistance screen. Similar to Zip6, Zip9 has also been shown to regulate zinc homeostasis and ZnT7 actively reduces cytoplasmic zinc concentration by its sequestration into the Golgi apparatus (Kirschke & Huang, 2003; Matsuura et al., 2009). It is likely that misregula-

tion of these proteins could also lead to elevated zinc levels in the cell cytoplasm, leading to observed resistance to CDK4/6i similar to that of SLC39A6 mutation. Our studies showed that the artificial elevation of intracellular zinc rescued CDK4/6i mediated cytostasis. Increased levels of intracellular labile zinc have been shown to inhibit cellular phosphatases such as PHLPP2 (PH domain leucine-rich repeat protein phosphatase) and trigger phosphorylation of Akt (activating the PI3k-Akt pathway) leading to drug resistance (Bafaro, Liu, Xu, & Dempski, 2017). A similar resistance mechanism of elevated Akt phosphorylation was recently observed in breast cancer patients who relapsed on a combination treatment ribociclib, letrozole and β-sparing P13Kα inhibitor piqray (Costa et al., 2019).

Taken together, our 3D phenotypic platform for identifying anti-cancer drug resistance brings context specific advantages over 2D platforms and might enable enrichment and detection of phenotypes lost in conventional 2D in-vitro drug resistance screens, important for a thorough understanding of the disease progression and therapeutic drug development.

6. ACKNOWLEDGEMENTS

We thank Jia Zhang for sgRNA plasmid cloning. We thank Doug Quackenbush and Tiffany Chu for their help with confocal experiments. We thank Frederick Lo for his help with image analysis. We thank James Giligan for help with the Agilent Bravo tool. We thank Glen Federe for assistance with sequencing the samples and analysis. We thank Ajay Vashist for his help and expertise in guiding us with membrane protein extraction. We thank Rajesh Nair and Bill Wackov with their help in zinc reconfirmation experiments. We thank Dr. Steve Bender and Dr. Zhizhong Li for their intellectual contribution and the support of GNF postdoc program for the successful completion of this work.

REFERENCES

Angus, L., Smid, M., Wilting, S. M., van Riet, J., Van Hoeck, A., Nguyen, L., . . . Martens, J. W. M. (2019). The genomic landscape of metastatic breast cancer highlights changes in mutation and signature frequencies. *Nature Genetics, 51*(10), 1450-1458. doi:10.1038/s41588-019-0507-7

Bacevic, K., Noble, R., Soffar, A., Ammar, O. W., Boszonyik, B., Prieto, S., . . . Fisher, D. (2017). Spatial competition constrains resistance to targeted cancer therapy. *Nature communications, 8*(1), 1995.

Bafaro, E., Liu, Y., Xu, Y., & Dempski, R. E. (2017). The emerging role of zinc transporters in cellular homeostasis and cancer. *Signal transduction and targeted therapy, 2*, 17029.

Chen, S., Sanjana, N. E., Zheng, K., Shalem, O., Lee, K., Shi, X., . . . Weissleder, R. (2015). Genome-wide CRISPR screen in a mouse model of tumor growth and metastasis. *Cell, 160*(6), 1246-1260.

Costa, C., Wang, Y., Ly, A., Hosono, Y., Ellen, M., Walmsley, C. S., . . . Juric, D. (2019). PTEN loss mediates clinical cross-resistance to CDK4/6 and PI3Kα inhibitors in breast cancer. *Cancer discovery*, CD-18-0830. doi:10.1158/2159-8290.cd-18-0830

Dai, X., Hua, T., & Hong, T. (2017). Integrated diagnostic network construction reveals a 4-gene panel and 5 cancer hallmarks driving breast cancer heterogeneity. *Scientific reports, 7*(1), 6827.

Garraway, L. A., & Jänne, P. A. (2012). Circumventing cancer drug resistance in the era of personalized medicine. *Cancer discovery, 2*(3), 214-226.

Grandhi, T. S. P., Potta, T., Nitiyanandan, R., Deshpande, I., & Rege, K. (2017). Chemomechanically engineered 3D organotypic platforms of bladder cancer dormancy and reactivation. *Biomaterials, 142*, 171-185.

Han, K., Pierce, S. E., Li, A., Spees, K., Anderson, G. R., Seoane, J. A., . . . Kamber, R. A. (2020). CRISPR screens in cancer spheroids identify 3D growth-specific vulnerabilities. *Nature, 580*(7801), 136-141.

Hoarau-Véchot, J., Rafii, A., Touboul, C., & Pasquier, J. (2018). Halfway between 2D and animal models: are 3D cultures the ideal tool to study cancer-microenvironment interactions? *International journal of molecular sciences, 19*(1), 181.

Horman, S. R., To, J., Lamb, J., Zoll, J. H., Leonetti, N., Tu, B., . . . Orth, A. P. (2017). Functional profiling of microtumors to identify cancer associated fibroblast-derived drug targets. *Oncotarget, 8*(59), 99913.

Housman, G., Byler, S., Heerboth, S., Lapinska, K., Longacre, M., Snyder, N., & Sarkar, S. (2014). Drug resistance in cancer: an overview. *Cancers, 6*(3), 1769-1792.

Imamura, Y., Mukohara, T., Shimono, Y., Funakoshi, Y., Chayahara, N., Toyoda, M., . . . Nakatsura, T. (2015). Comparison of 2D-and 3D-culture models as drug-testing platforms in breast cancer. *Oncology reports, 33*(4), 1837-1843.

Jove, M., Spencer, J. A., Hubbard, M. E., Holden, E. C., D O'Dea, R., Brook, B. S., . . . Twelves, C. J. (2019). Cellular uptake and efflux of palbociclib in vitro in single cell and spheroid models. *Journal of Pharmacology and Experimental Therapeutics*, jpet. 119.256693.

Kasper, G., Weiser, A. A., Rump, A., Sparbier, K., Dahl, E., Hartmann, A., . . . Lehmann, K. (2005). Expression levels of the putative zinc transporter LIV-1 are associated with a better outcome of breast cancer patients. *International journal of cancer, 117*(6), 961-973.

Khleif, S. N., DeGregori, J., Yee, C. L., Otterson, G. A., Kaye, F. J., Nevins, J. R., & Howley, P. M. (1996). Inhibition of cyclin D-CDK4/CDK6 activity is associated with an E2F-mediated induction of cyclin kinase inhibitor activity. *Proceedings of the National Academy of Sciences, 93*(9), 4350-4354.

Kim, C. H., Kim, J. H., Moon, S. J., Chung, K. C., Hsu, C. Y., Seo, J. T., & Ahn, Y. S. (1999). Pyrithione, a zinc ionophore, inhibits NF-κB activation. *Biochemical and biophysical research communications, 259*(3), 505-509.

Kirschke, C. P., & Huang, L. (2003). ZnT7, a novel mammalian zinc transporter, accumulates zinc in the Golgi apparatus. *Journal of Biological Chemistry, 278*(6), 4096-4102.

Knudsen, E. S., & Witkiewicz, A. K. (2017a). The strange case of CDK4/6 inhibitors: mechanisms, resistance, and combination strategies. *Trends in Cancer, 3*(1), 39-55.

Knudsen, E. S., & Witkiewicz, A. K. (2017b). The Strange Case of CDK4/6 Inhibitors: Mechanisms, Resistance, and Combination Strategies. *Trends in Cancer*.

Kwapisz, D. (2017). Cyclin-dependent kinase 4/6 inhibitors in breast cancer: palbociclib, ribociclib, and abemaciclib. *Breast cancer research and treatment, 166*(1), 41-54.

Liston, D. R., & Davis, M. (2017). Clinically relevant concentrations of anticancer drugs: a guide for nonclinical studies. *Clinical cancer research, 23*(14), 3489-3498.

Llanos, S., Megias, D., Blanco-Aparicio, C., Hernández-Encinas, E., Rovira, M., Pietrocola, F., & Serrano, M. (2019). Lysosomal trapping of palbociclib and its functional implications. *Oncogene, 38*(20), 3886-3902. doi:10.1038/s41388-019-0695-8

Loeb, L. A. (2016). Human cancers express a mutator phenotype: hypothesis, origin, and consequences. *Cancer research, 76*(8), 2057-2059.

Loeb, L. A., Loeb, K. R., & Anderson, J. P. (2003). Multiple mutations and cancer. *Proceedings of the National Academy of Sciences, 100*(3), 776-781.

Lopez, V., & Kelleher, S. L. (2010). Zip6-attenuation promotes epithelial-to-mesenchymal transition in ductal breast tumor (T47D) cells. *Experimental cell research, 316*(3), 366-375.

Ma, X., Ma, Q., Liu, J., Tian, Y., Wang, B., Taylor, K. M., . . . Meng, L. (2009). Identification of LIV1, a putative zinc transporter gene responsible for HDACi-induced apoptosis, using a functional gene screen approach. *Molecular cancer therapeutics, 8*(11), 3108-3116.

Matsuura, W., Yamazaki, T., Yamaguchi-Iwai, Y., Masuda, S., Nagao, M., Andrews, G. K., & Kambe, T. (2009). SLC39A9 (ZIP9) regulates zinc homeostasis in the secretory pathway: characterization of the ZIP subfamily I protein in vertebrate cells. *Bioscience, biotechnology, and biochemistry, 73*(5), 1142-1148.

McDermott, M., Eustace, A., Busschots, S., Breen, L., Clynes, M., O'Donovan, N., & Stordal, B. (2014). In vitro development of chemotherapy and targeted therapy drug-resistant cancer cell lines: a practical guide with case studies. *Frontiers in oncology, 4*, 40.

Pao, W., Miller, V. A., Politi, K. A., Riely, G. J., Somwar, R., Zakowski, M. F., . . . Varmus, H. (2005). Acquired resistance of lung adenocarcinomas to gefitinib or erlotinib is associated with a second mutation in the EGFR kinase domain. *PLoS medicine, 2*(3), e73.

Pernas, S., Tolaney, S. M., Winer, E. P., & Goel, S. (2018). CDK4/6 inhibition in breast cancer: current practice and future directions. *Therapeutic Advances in Medical Oncology, 10*, 1758835918786451.

Pervez, S., & Khan, H. (2007). Infiltrating ductal carcinoma breast with central necrosis closely mimicking ductal carcinoma in situ (comedo type): a case series. *Journal of medical case reports, 1*(1), 83.

Sabbah, M., Courilleau, D., Mester, J., & Redeuilh, G. (1999). Estrogen induction of the cyclin D1 promoter: involvement of a cAMP response-like element. *Proceedings of the National Academy of Sciences, 96*(20), 11217-11222.

Sinn, B. V., Fu, C., Lau, R., Litton, J., Tsai, T.-H., Murthy, R., . . . Murthy, R. (2019). SET ER/PR: a robust 18-gene predictor for sensitivity to endocrine therapy for metastatic breast cancer. *NPJ breast cancer, 5*(1), 16.

Szlachta, K., Kuscu, C., Tufan, T., Adair, S. J., Shang, S., Michaels, A. D., . . . Liu, L. (2018). CRISPR knockout screening identifies combinatorial drug targets in pancreatic cancer and models cellular drug response. *Nature communications, 9*(1), 1-13.

Tchoryk, A., Taresco, V., Argent, R. H., Ashford, M., Gellert, P. R., Stolnik, S., . . . Garnett, M. C. (2019). Penetration and Uptake of Nanoparticles in 3D Tumor Spheroids. *Bioconjugate Chemistry, 30*(5), 1371-1384.

Tomes, L., Emberley, E., Niu, Y., Troup, S., Pastorek, J., Strange, K., . . . Watson, P. H. (2003). Necrosis and hypoxia in invasive breast carcinoma. *Breast cancer research and treatment, 81*(1), 61-69.

Turner, N. C., Slamon, D. J., Ro, J., Bondarenko, I., Im, S.-A., Masuda, N., . . . Verma, S. (2018). Overall survival with palbociclib and fulvestrant in advanced breast cancer. *New England Journal of Medicine, 379*(20), 1926-1936.

FIGURE LEGENDS

Figure 1. ER+ Her2- T47D-Cas9 cells form 3D MCTS and mimic solid tumor biology. (A) 2500 T47D-Cas9 cells plated in Corning 384w Ultralow Attachment plates form 3D spheroids that continue to grow over time (day 4-20) as indicated by volumetric increase measured out to day 20. (B) H&E and Anti-Ki67 antibody staining of spheroid sections identify zones of necrosis and active proliferation (C) Treatment with the CDK4/6i CDK4/6i results in a dose-dependent reduction in the T47D-Cas9 spheroid volume quantified on day 20. Transmitted light images of day 4 and day 20 spheroids before and after drug exposure are shown. (D) 1 μM CDK4/6i treatment of 2500-cell T47D 3D MCTS caused its accumulation in punctate bodies in the cell cytoplasm over 12 hours in the spheroid shell (50 μm deep into the spheroid shell). The specific z-section situated 50 μm deep into the spheroid shell of the 12 hour image reveals punctate bodies (highlighted with arrows) highlighting (****$p < 0.0001$, One-way ANOVA, comparison to 0 μM drug control). Scale bar = 100 μm

Figure 2. 3D spheroid sensitivity to CDK4/6i is abrogated after retinoblastoma (RB1) deletion. (A) Stable cell clones, prepared after retinoblastoma deletion using the CRISPR-Cas9 machinery, form 3D spheroids that are resistant to CDK4/6i at a concentration significantly higher than GI(0). (B) RB1 knockouts (RB1 KOs) are resistant to cytostasis in 2D (quantified after 6 days) . (C) Spheroids formed by titrating low numbers of RB1 knockout cells (160 cells and 2 cells) within 2500 cell spheroid (scrambled control) exposed to 10 μM CDK4/6i for 24 days. Spheroid size estimated over 24 days for different cell titrations indicated delayed growth at low resistant cell numbers. (D) Ki67+ staining of resistant:sensitive spheroid sections after 24 days of drug treatment. (E) Sequencing analysis of spheroids to characterize the distribution of RB1 KOs compared to scrambled controls after 24 days of enrichment under drug stress. ****$p < 0.0001$, One-way ANOVA, calculated in comparison to live and scrambled controls. Scale bar = 100 μm

Figure 3. Genome-wide screening identifies known and novel resistance mechanisms against CDK4/6 inhibitors. (A) Assay workflow for genome-wide pooled in-vitro CRISPR screening: 2D vs 3D CDK4/6i enrichment assays were performed by generating stable cell clones with genome-wide knockouts via lentiviral transduction. T47D-Cas9 genome-wide KO cells were assembled into 3D spheroids before addition of drug. A control 2D experiment to understand temporal changes in knockout enrichment in 2D over 28 days was performed simultaneously. Periodic sampling of the cells was performed on days 10, 16, 22 and 28. (B) Representative images of two distinct modes of positive enrichment observed during the experiment (dumble-shaped enrichment and total spheroid volumetric increase) compared to unenriched controls. (C) Heat map showing the 20 most enriched genes in 3D pooled CRISPR screen and their comparison to 2D enriched hits across different time points. (D) Pooled in-vitro 3D CRISPR screen identified unique genes (red arrows) as novel targets that induce CDK4/6i resistance, RB1 deletion was identified in 3D enrichment assay (day 10; 2D vs 3D comparison). Lower LogP values indicate significant enrichment over background. Bounds on the quadrants are for visualization only.

Figure 4. SLC39A6-edited T47D cells resist CDK4/6i induced cytostasis. (A) Western blotting of membrane enriched fractions of SLC-KO2, KO4 and scrambled control cells indicated evidence of a truncated SLC39A6 protein (~15.9 KDa band). (B) Growth inhibition values estimated after 6 day treatment of T47D SLC-KO2, –KO4 and scrambled control cells with a 10-point dilution of CDK4/6i in 2D. (C) 3D spheroids generated with SLC-KO2 and –KO4 cells showed slight yet significant increases in spheroid volume over scrambled control cells under monotherapy CDK4/6i treatment (D) 2D fulvesterant treatment (E) 3D fulvesterant treatment and (F) and combination CDK4/6i/fulvesterant treatment in 3D and 2D. (representative images shown). ****$p < 0.0001$, ***$p<0.005$, **$p<0.01$, *$p<0.05$ One-way ANOVA compared to the indicated control. Scale bar = 100 μm

Figure 5. Elevation of intracellular zinc causes resistance to CDK4/6i-mediated cytostasis. (A) Incubation of T47D scrambled control cells with zinc sulfate and pyrithione led to a dose-dependent increase in Fluozin3 fluorescence. Histogram plot shows a normalized reading across the three conditions. Exogenous zinc delivery to (B) T47D scrambled control cells and (C) MCF7-Cas9 cells via pyrithione rescues CDK4/6i mediated cytostasis over 6 days as well ****$p < 0.0001$, ***$p<0.005$, **$p<0.01$, *$p<0.05$ One-way ANOVA compared to the indicated control.

FIGURES

Figure 1

A.

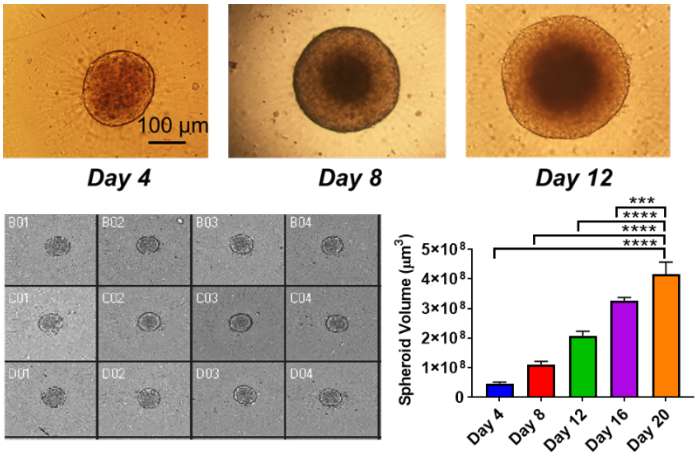

B.

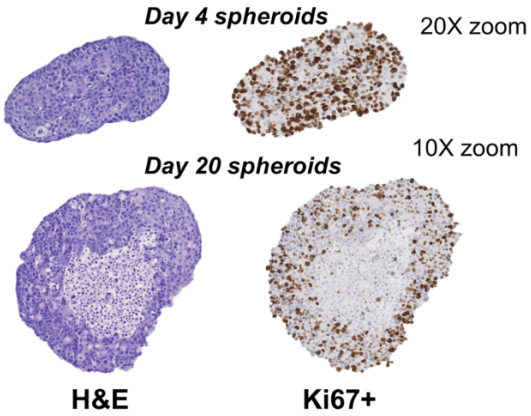

C.

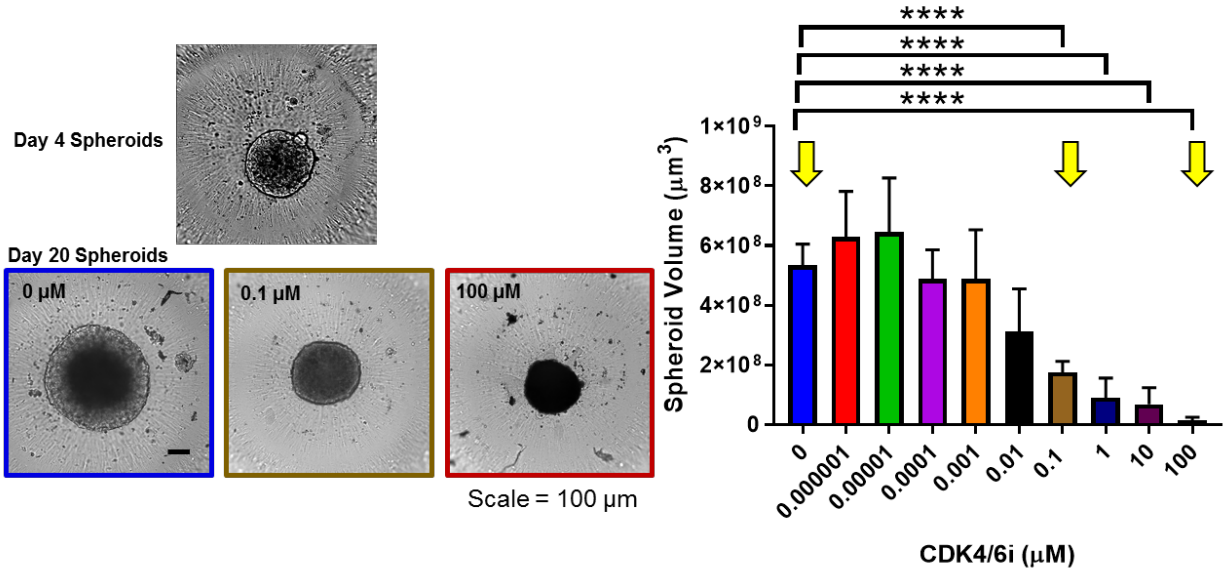

D.

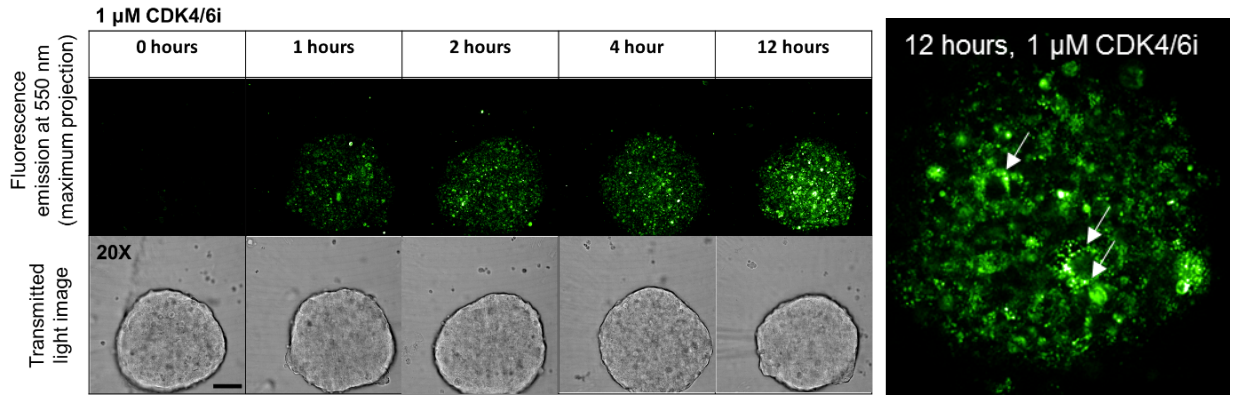

Figure 1. ER+ Her2- T47D-Cas9 cells form 3D MCTS and mimic solid tumor biology. (A) 2500 T47D-Cas9 cells plated in Corning 384w Ultralow Attachment plates form 3D spheroids that continue to grow over time (day 4-20) as indicated by volumetric increase measured out to day 20. (B) H&E and Anti-Ki67 antibody staining of spheroid sections identify zones of necrosis and active proliferation (C) Treatment with the CDK4/6i CDK4/6i results in a dose-dependent reduction in the T47D-Cas9 spheroid volume quantified on day 20. Transmitted light images of day 4 and day 20 spheroids before and after drug exposure are shown. (D) 1 µM CDK4/6i treatment of 2500-cell T47D 3D MCTS caused its accumulation in punctate bodies in the cell cytoplasm over 12 hours in the spheroid shell (50 µm deep into the spheroid shell). The specific z-section situated 50 µm deep into the spheroid shell of the 12 hour image reveals punctate bodies (highlighted with arrows) highlighting (****$p < 0.0001$, One-way ANOVA, comparison to 0 µM drug control). Scale bar = 100 µm

Figure 2.

A.

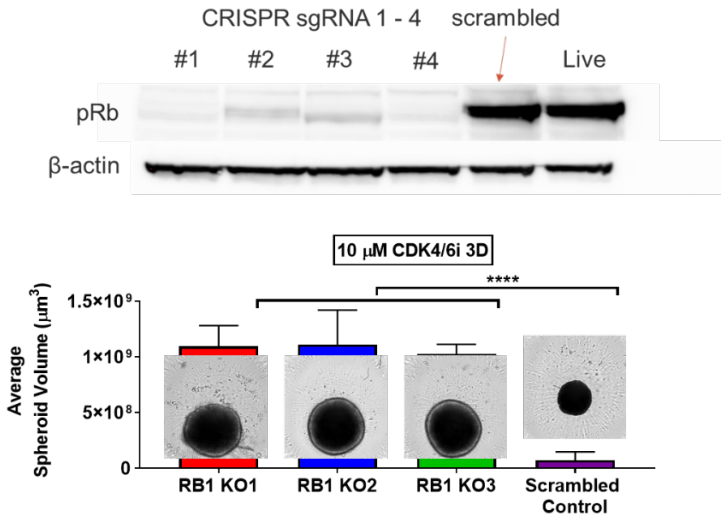

B

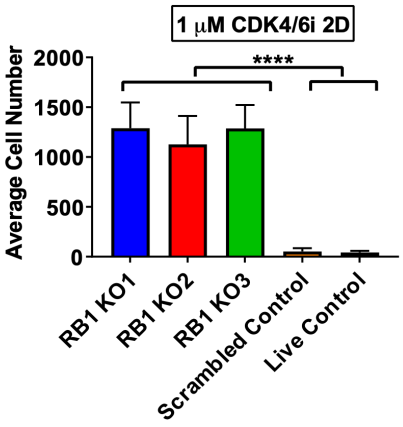

C

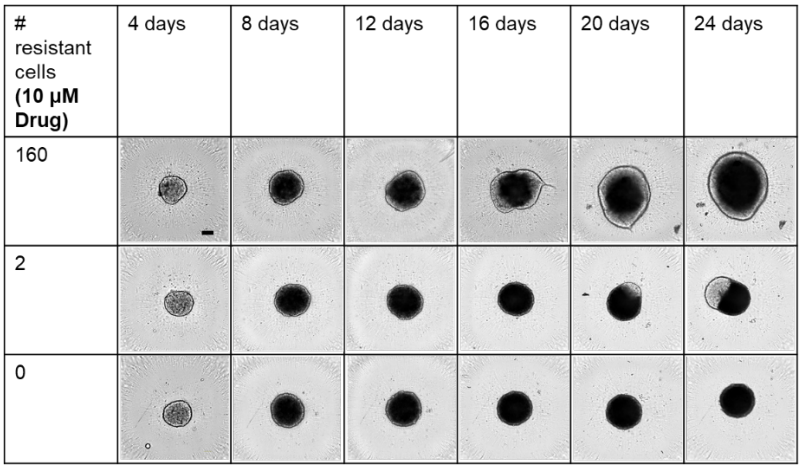

D

E

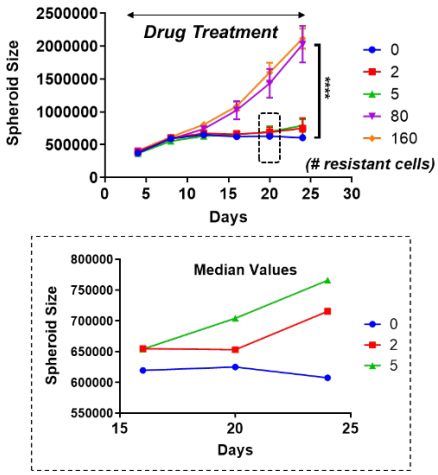

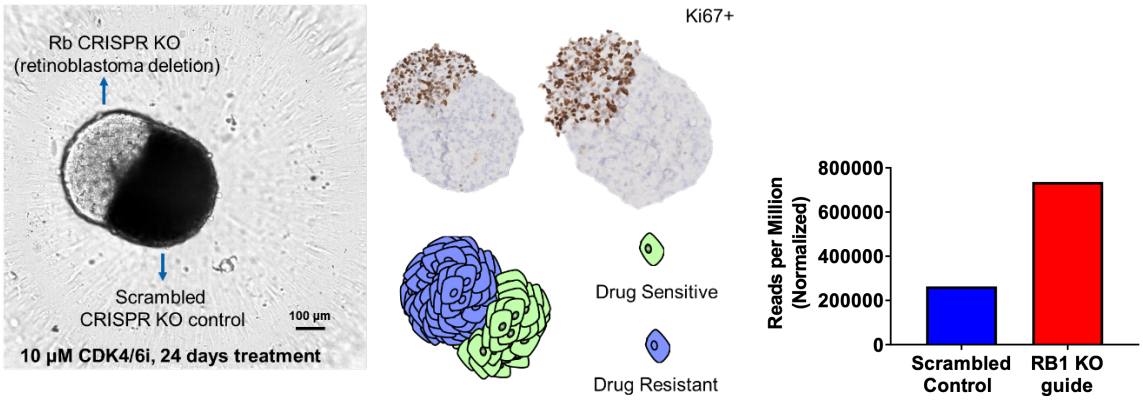

Figure 2. 3D spheroid sensitivity to CDK4/6i is abrogated after retinoblastoma (RB1) deletion. (A) Stable cell clones, prepared after retinoblastoma deletion using the CRISPR-Cas9 machinery, form 3D spheroids that are resistant to CDK4/6i at a concentration significantly higher than GI(0). (B) RB1 knockouts (RB1 KOs) are resistant to cytostasis in 2D (quantified after 6 days) . (C) Spheroids formed by titrating low numbers of RB1 knockout cells (160 cells and 2 cells) within 2500 cell spheroid (scrambled control) exposed to 10 μM CDK4/6i for 24 days. Spheroid size estimated over 24 days for different cell titrations indicated delayed growth at low resistant cell numbers. (D) Ki67+ staining of resistant:sensitive spheroid sections after 24 days of drug treatment. (E) Sequencing analysis of spheroids to characterize the distribution of RB1 KOs compared to scrambled controls after 24 days of enrichment under drug stress. ****$p < 0.0001$, One-way ANOVA, calculated in comparison to live and scrambled controls. Scale bar = 100 μm

Figure 3.

A

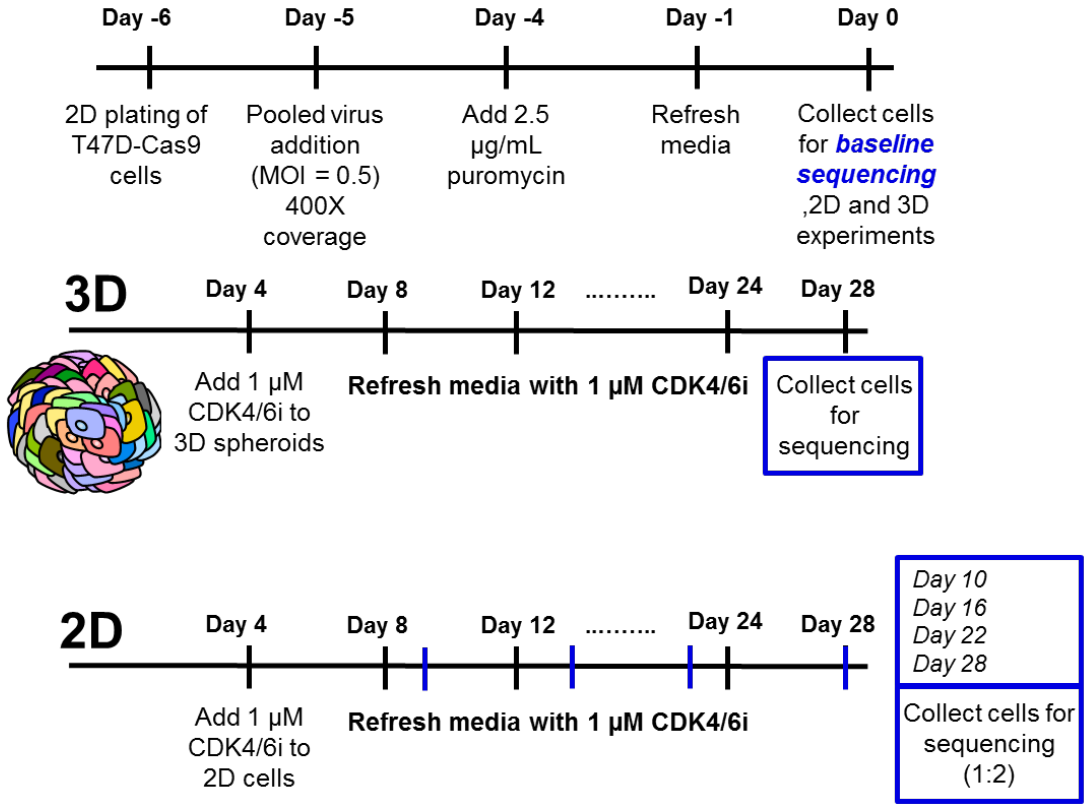
Day -6
Day -5
Day -4
Day -1
Day 0
2D plating of T47D-Cas9 cells
Pooled virus addition (MOI = 0.5) 400X coverage
Add 2.5 µg/mL puromycin
Refresh media
Collect cells for baseline sequencing ,2D and 3D experiments
3D
Day 4
Day 8
Day 12
.....
Day 24
Day 28
Add 1 µM CDK4/6i to 3D spheroids
Refresh media with 1 µM CDK4/6i
Collect cells for sequencing
2D
Day 4
Day 8
Day 12
.....
Day 24
Day 28
Day 10
Day 16
Day 22
Day 28
Add 1 µM CDK4/6i to 2D cells
Refresh media with 1 µM CDK4/6i
Collect cells for sequencing (1:2)

B

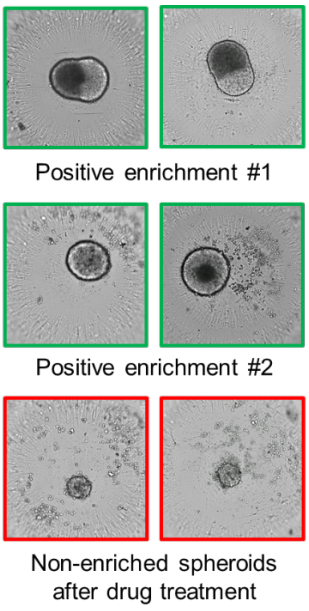
Positive enrichment #1
Positive enrichment #2
Non-enriched spheroids after drug treatment

C

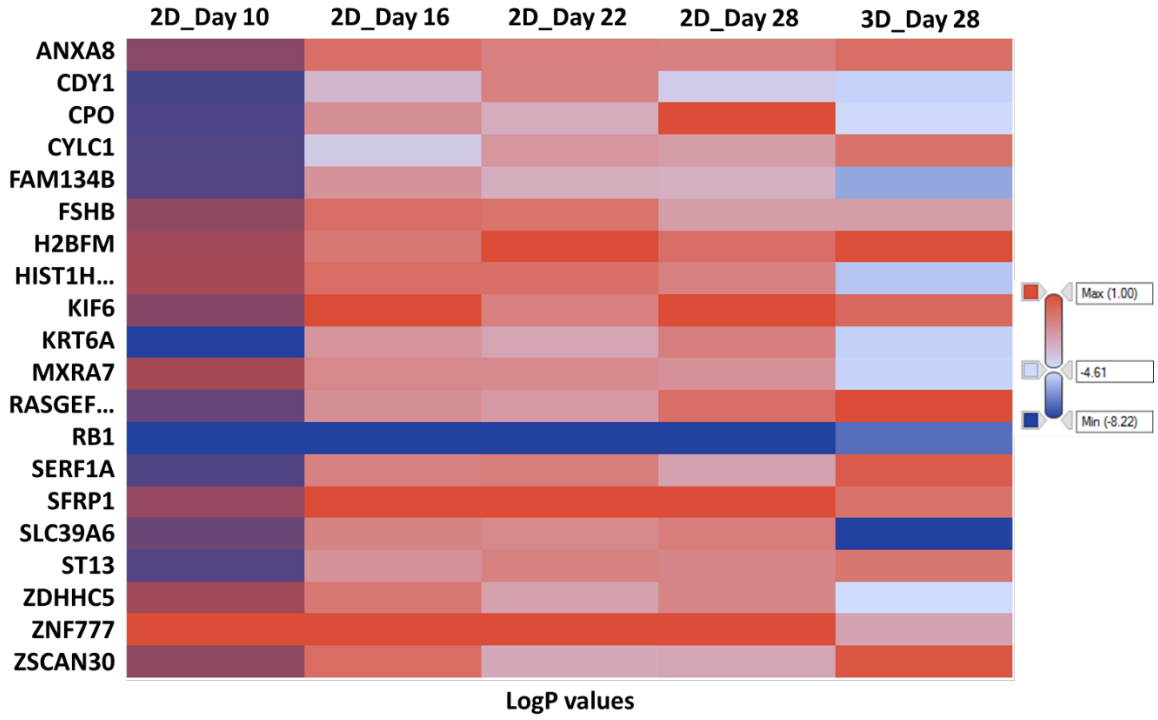
2D_Day 10
2D_Day 16
2D_Day 22
2D_Day 28
3D_Day 28
ANXA8
CDY1
CPO
CYLC1
FAM134B
FSHB
H2BFM
HIST1H...
KIF6
KRT6A
MXRA7
RASGEF...
RB1
SERF1A
SFRP1
SLC39A6
ST13
ZDHHC5
ZNF777
ZSCAN30
Max (1.00)
-4.61
Min (-8.22)
LogP values

D

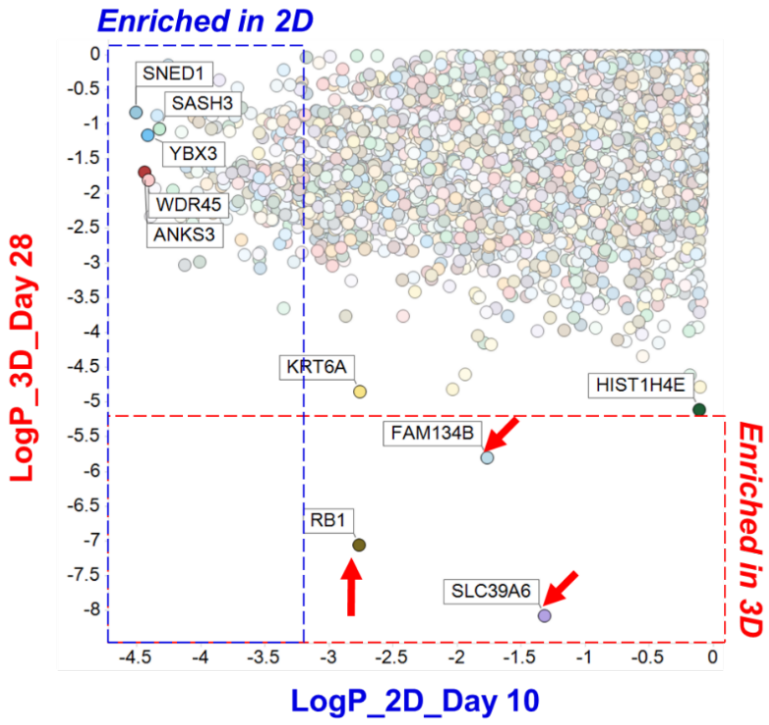
Enriched in 2D
SNED1
SASH3
YBX3
WDR45
ANKS3
KRT6A
HIST1H4E
FAM134B
RB1
SLC39A6
Enriched in 3D
LogP_3D_Day 28
LogP_2D_Day 10
0
-0.5
-1
-1.5
-2
-2.5
-3
-3.5
-4
-4.5
-5
-5.5
-6
-6.5
-7
-7.5
-8
-4.5
-4
-3.5
-3
-2.5
-2
-1.5
-1
-0.5
0

Figure 3. Genome-wide screening identifies known and novel resistance mechanisms against CDK4/6 inhibitors. (A) Assay workflow for genome-wide pooled in-vitro CRISPR screening: 2D vs 3D CDK4/6i enrichment assays were performed by generating stable cell clones with genome-wide knockouts via lentiviral transduction. T47D-Cas9 genome-wide KO cells were assembled into 3D spheroids before addition of drug. A control 2D experiment to understand temporal changes in knockout enrichment in 2D over 28 days was performed simultaneously. Periodic sampling of the cells was performed on days 10, 16, 22 and 28. (B) Representative images of two distinct modes of positive enrichment observed during the experiment (dumble-shaped enrichment and total spheroid volumetric increase) compared to unenriched controls. (C) Heat map showing the 20 most enriched genes in 3D pooled CRISPR screen and their comparison to 2D enriched hits across different time points. (D) Pooled in-vitro 3D CRISPR screen identified unique genes (red arrows) as novel targets that induce CDK4/6i resistance, RB1 deletion was identified in 3D enrichment assay (day 10; 2D vs 3D comparison). Lower LogP values indicate significant enrichment over background. Bounds on the quadrants are for visualization only.

Figure 4.

A

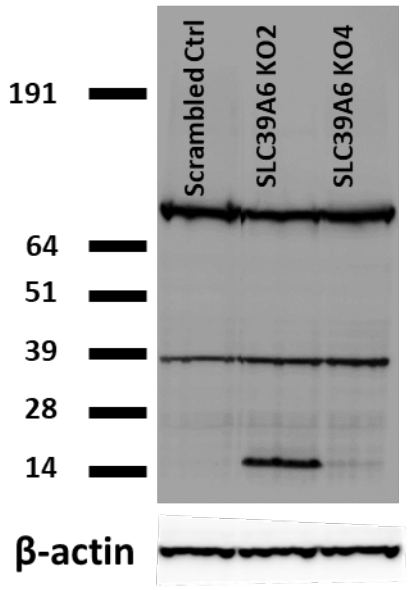

B

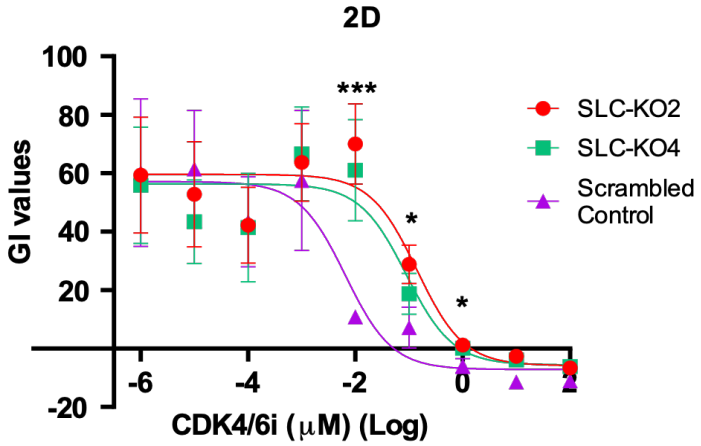

C

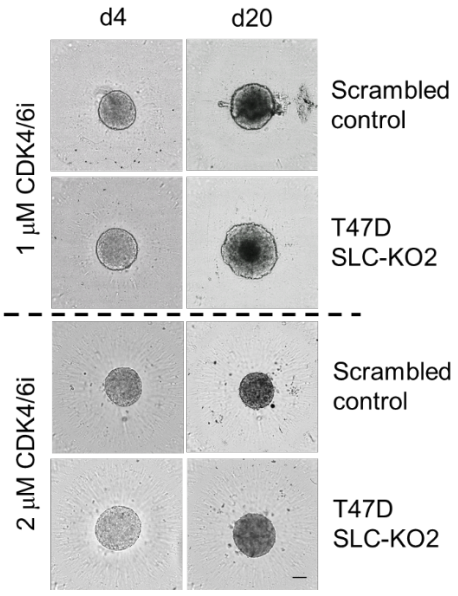

D

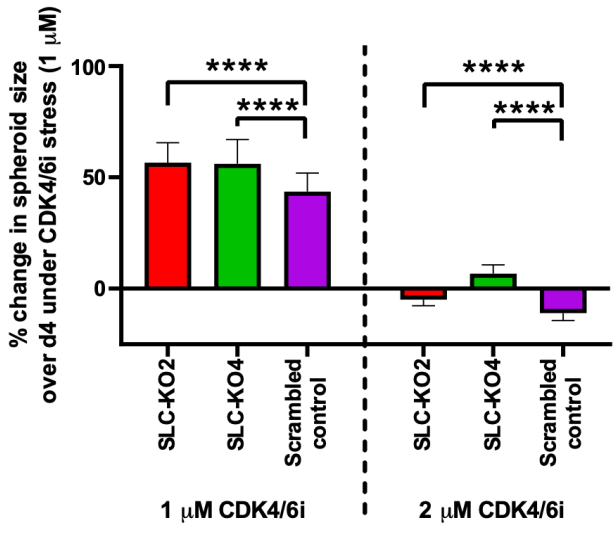

E

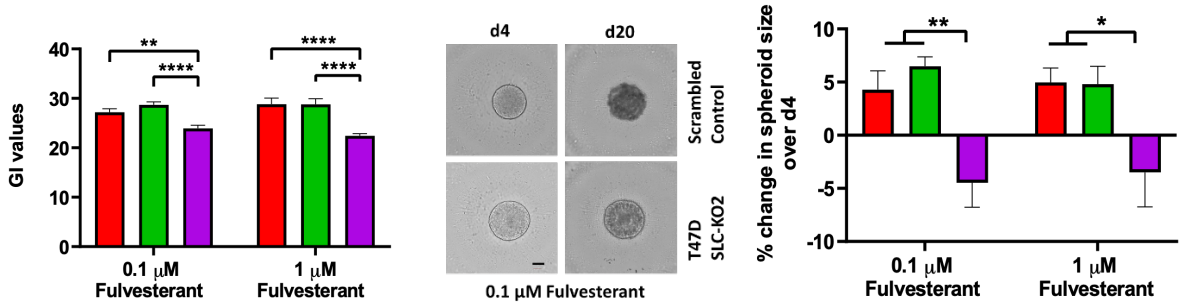

F

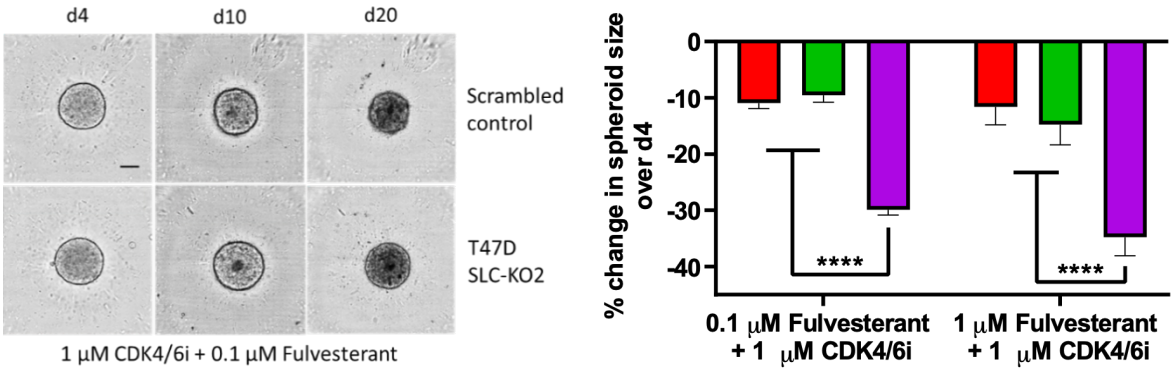

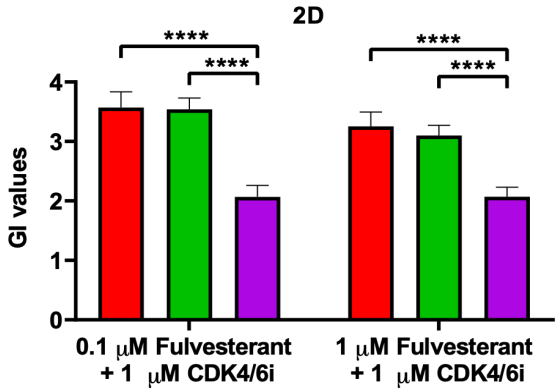

Figure 4. SLC39A6-edited T47D cells resist CDK4/6i induced cytostasis. (A) Western blotting of membrane enriched fractions of SLC-KO2, KO4 and scrambled control cells indicated evidence of a truncated SLC39A6 protein (~15.9 KDa band). (B) Growth inhibition values estimated after 6 day treatment of T47D SLC-KO2, –KO4 and scrambled control cells with a 10-point dilution of CDK4/6i in 2D. (C) 3D spheroids generated with SLC-KO2 and –KO4 cells showed slight yet

significant increases in spheroid volume over scrambled control cells under monotherapy CDK4/6i treatment (D) 2D fulvesterant treatment (E) 3D fulvesterant treatment and (F) and combination CDK4/6i/fulvesterant treatment in 3D and 2D. (representative images shown). ****p < 0.0001, ***p<0.005, **p<0.01, *p<0.05 One-way ANOVA compared to the indicated control. Scale bar = 100 μm

Figure 5.

A

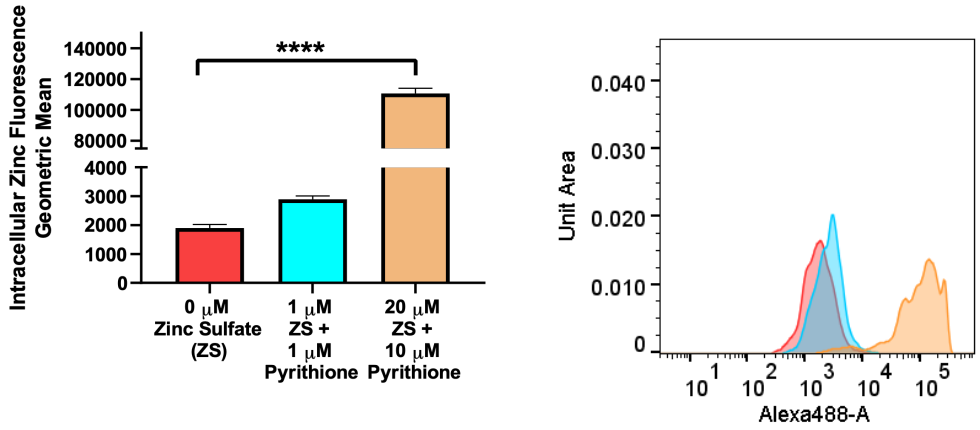
Intracellular Zinc Fluorescence
Geometric Mean
140000
120000
100000
80000
4000
3000
2000
1000
0
****
0 μM
Zinc Sulfate
(ZS)
1 μM
ZS +
1 μM
Pyrithione
20 μM
ZS +
10 μM
Pyrithione
Unit Area
0.040
0.030
0.020
0.010
0
10 1
10 2
10 3
10 4
10 5
Alexa488-A

B

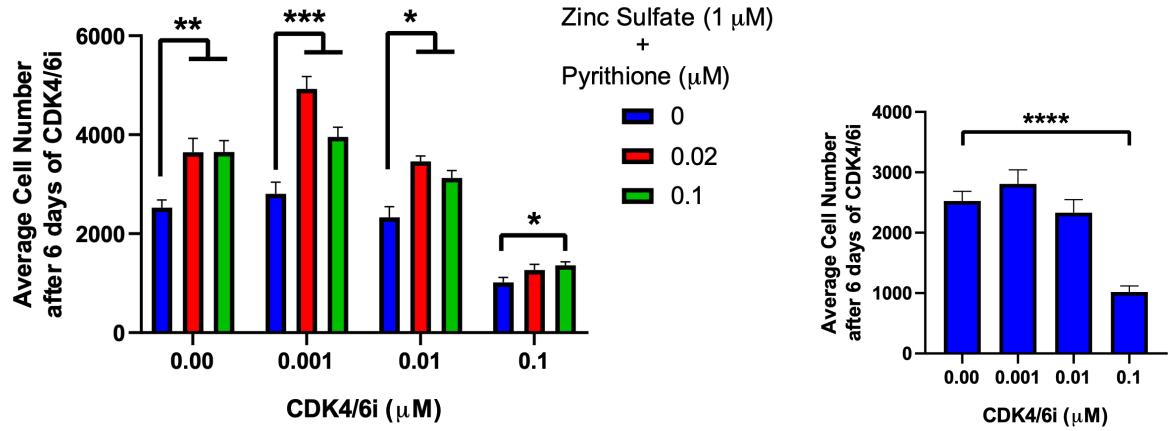
Average Cell Number
after 6 days of CDK4/6i
6000
4000
2000
0
**
***
*
*
0.00
0.001
0.01
0.1
CDK4/6i (μM)
Zinc Sulfate (1 μM)
+
Pyrithione (μM)
0
0.02
0.1
Average Cell Number
after 6 days of CDK4/6i
4000
3000
2000
1000
0
****
0.00
0.001
0.01
0.1
CDK4/6i (μM)

C

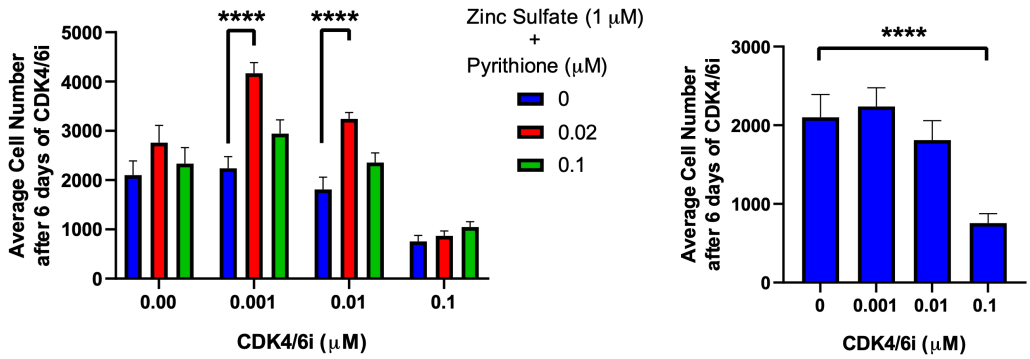
Average Cell Number
after 6 days of CDK4/6i
5000
4000
3000
2000
1000
0
****
****
0.00
0.001
0.01
0.1
CDK4/6i (μM)
Zinc Sulfate (1 μM)
+
Pyrithione (μM)
0
0.02
0.1
Average Cell Number
after 6 days of CDK4/6i
3000
2000
1000
0
****
0
0.001
0.01
0.1
CDK4/6i (μM)

Figure 5. Elevation of intracellular zinc causes resistance to CDK4/6i-mediated cytostasis. (A) Incubation of T47D scrambled control cells with zinc sulfate and pyrithione led to a dose-dependent increase in Fluozin3 fluorescence. Histogram plot shows a normalized reading across the three conditions. Exogenous zinc delivery to (B) T47D scrambled control cells and (C) MCF7-Cas9 cells via pyrithione rescues CDK4/6i mediated cytostasis over 6 days as well ****$p < 0.0001$, ***$p<0.005$, **$p<0.01$, *$p<0.05$ One-way ANOVA compared to the indicated control.